The IRM Quarterly
Fall 2023, Vol. 33 No. 3
ISSN: 2152-1972

Inside...

Principles of statistical evaluation of anisotropy of magnetic susceptibility – Specimen level

František Hrouda[1,2]
hrouda@agico.cz

Josef Ježek[2]
jezek@natur.cuni.cz

Martin Chadima[1,3]
chadima@agico.cz

Jan Studýnka[1]
studynka@agico.cz

[1]AGICO, Inc.; [2]Faculty of Science, Charles University, Prague; [3]Institute of Geology, Academy of Sciences, Prague.

1. Introduction

Theory of the low-field anisotropy of magnetic susceptibility (AMS) assumes a linear relationship between induced magnetization and magnetizing field, described as $\boldsymbol{M} = \mathbf{k}\,\boldsymbol{H}$, where $\boldsymbol{M}$ is the magnetization vector, $\boldsymbol{H}$ is the vector of the intensity of the external magnetizing field, and $\mathbf{k}$ is the symmetric second rank tensor of magnetic susceptibility. The tensor $\mathbf{k}$ is most frequently determined through susceptibility measurements in at least six, but often substantially more than six directions. Configuration of the set of measuring directions, called the measuring design, is conveniently described by the design matrix $\mathbf{A}$ (for details of its construction see, e.g., Hext, 1963; Jelínek, 1977; Studýnka et al., 2014).

The susceptibility tensor is estimated by means of linear regression and the least squares method. The vector of six independent elements of the susceptibility tensor ($\boldsymbol{k}_v$) is calculated as (Hext, 1963; Jelínek, 1977)

$$\boldsymbol{k}_v = (\mathbf{A}^T\mathbf{A})^{-1}\mathbf{A}^T\boldsymbol{k}_d$$

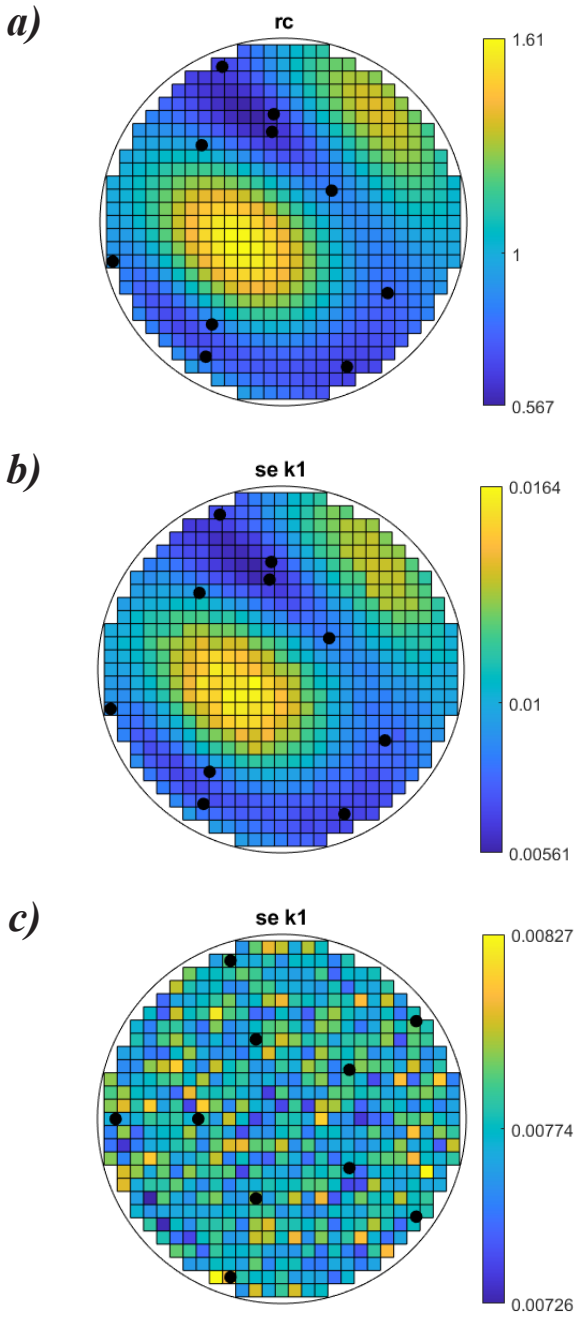

Figure 1: (a) A non-rotatable design consisting of 10 randomly chosen directions with colour coded rotatability coefficient. Measuring directions are denoted by full black circles. (b) Simulated standard error of the maximum susceptibility of the above design. (c) Simulated standard error of the maximum susceptibility using rotatable Hext 10 measuring design. Equal-area projection on lower hemisphere, instrument coordinate system.

cont'd. on pg. 12...

Visiting Fellow Reports

Micromagnetic Tomography of Paleoarchean dolerite dykes from Isua, Greenland- What tiny magnetite grains can tell us about the early days of the geomagnetic field

R.A. de Boer
Utrecht University
r.a.deboer1@uu.nl

Introduction

In August 2022 I visited the Institute for Rock Magnetism on a Magnetic Microscopy Fellowship, to use the quantum diamond microscope (QDM) for surface magnetometry. I am a PhD candidate at the paleomagnetic laboratory Fort Hoofddijk of Utrecht University, where I am part of a team that develops the novel method Micromagnetic Tomography (MMT; de Groot et al., 2018, 2021). This method can be used to extract reliable measurements of the past geomagnetic field by studying the magnetic properties of individual magnetic carriers.

For a first geological application of Micromagnetic Tomography, I use Paleoarchean samples from Isua, Greenland that were collected by Claire Nichols (University of Oxford). These samples, in spite of their apparent petrological and geochemical similarity, reveal radically different magnetic behavior. Understanding the difference in paleomagnetic recording properties between the samples is not easily resolved by traditional bulk paleomagnetic measurements. We aim to use MMT in an attempt to unravel the behavior of the complex geomagnetic field of the Paleoarchean.

Geological setting

Claire Nichols and colleagues organized two field expeditions in the summer of 2018 and 2019 to sample various Archean units in the Isua Supracrustal Belt, West Greenland. Amongst others, they sampled a (meta-)dolerite dyke swarm of ~3.5 Ga (Nutman et al., 2004), the locations of the sampled dykes are indicated in Figure 1. Dyke 6A experienced metamorphic conditions of 1.5-6 kbar and 400-500°C, while dyke 8A experienced lower grade metamorphic conditions of 1.5-4 kbar and 360-400°C (Arai et al., 2015). Since these dykes are part of the same dyke swarm they are expected to have similar capabilities for recording Earth's magnetic field, however, this is not confirmed by traditional paleomagnetic bulk analyses. Samples from dyke 6A show stable magnetic behavior, while samples from dyke 8A produce enigmatic results, see Figure 2 (Nichols et al., 2023, in review).

The inconsistency in magnetic behavior can potentially be attributed to variations in size, shape, and abundance of the magnetic minerals throughout the dykes. An in-depth MMT study might confirm a consistent difference in rock magnetic properties between the two dykes. It could aid in separating a primary (metamorphic) signal from potential later overprints in the magnetic carriers, as well as retrieving a magnetic direction from the samples that fail to produce reliable directions using bulk

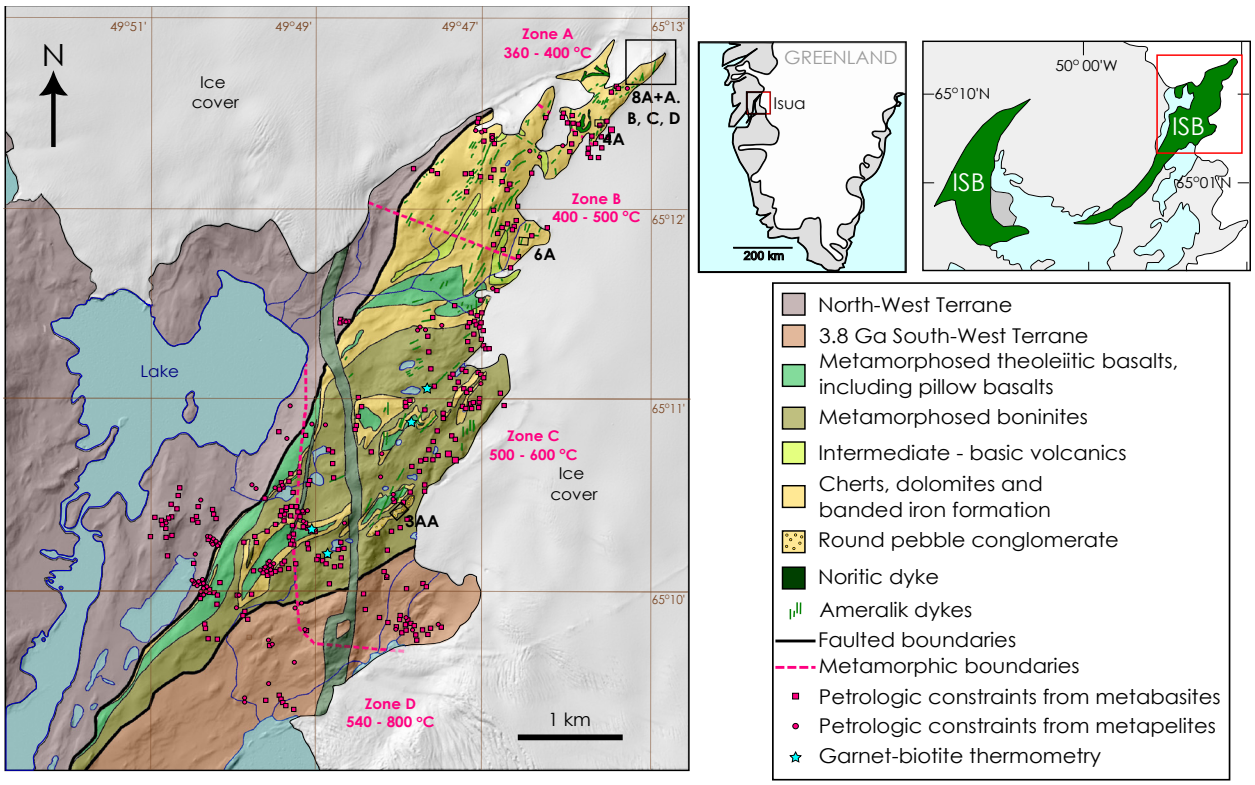

Figure 1: Geological map of the field area depicting the northeastern part of the Isua Supracrustal belt, Greenland, from Nichols et al. (2023, in review). Surface magnetometry was applied to samples from sites 6A and 8A.

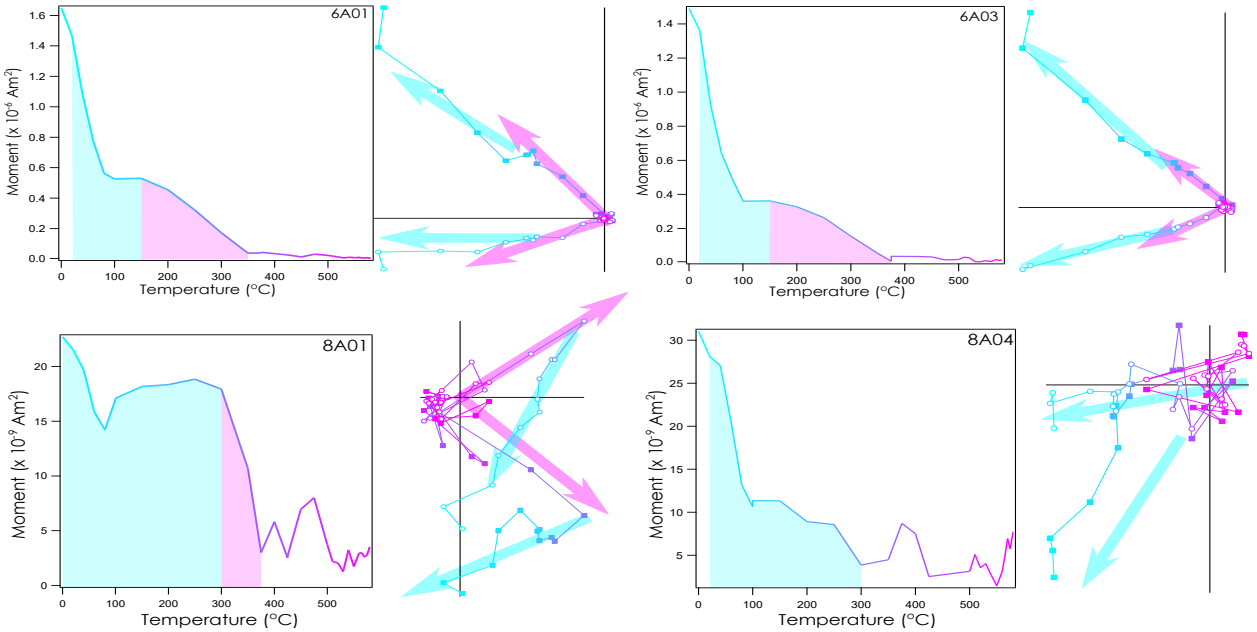

Figure 2: Representative demagnetization behavior of dykes 6A and 8A from Nichols et al., (2023, in review). Dyke 6A shows stable magnetic behavior and contains a single direction of dec. 321°/ inc. 29°. Dyke 8A exhibits less stable magnetic behavior and the HT component defines a direction of dec. 120°/ inc. -53°.

paleomagnetic methods.

Methods

Micromagnetic Tomography is a method that combines magnetic surface scans (using the QDM) with spatial and dimensional data (using nanoCT imaging) to obtain the individual magnetic moment per magnetic carrier. In traditional paleomagnetic analyses, thousands of magnetic particles in a bulk sample are measured as a single assemblage to determine the direction and strength of the magnetic field at the time of their formation. The presence of a number of magnetically unstable grains may hamper a reliable determination of the paleomagnetic information stored in bulk samples, even if reliable magnetic carriers are present. An important advantage of MMT as opposed to traditional bulk analyses is the distinction that can be made between reliable and unreliable magnetic recorders. By discarding the latter from the magnetic signal, MMT could improve the interpretation of magnetic signals that were previously too complex to interpret.

At the IRM I conducted surface magnetometry with the QDM for samples from both dyke 6A and dyke 8A in their pristine state (NRM) and after thermal and alternating field demagnetization steps. The demagnetization steps enable interpreting the magnetic signal of groups of grains with consistent behavior independently of other, inconsistent magnetic grains in the sample. The desired outcome of this study is that a common true mean direction is retrieved from well-behaved magnetic grains, in samples for which bulk measurements fail to produce reliable paleomagnetic data.

Results

Figure 3 shows surface magnetometry data obtained with the QDM. Two samples from dyke 6A were used, as well as two samples from dyke 8A. After measuring each sample in its pristine state (NRM), the samples

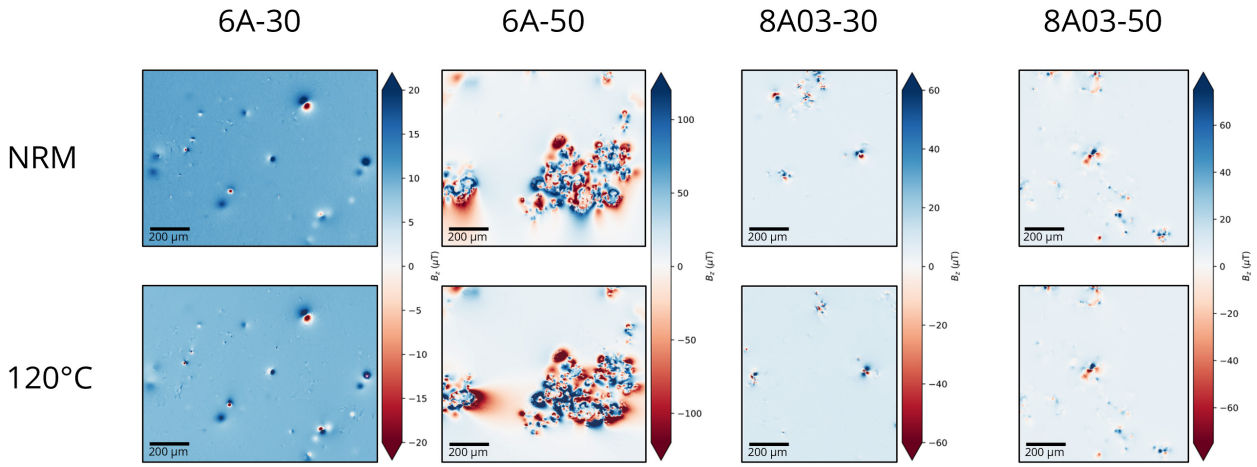

Figure 3: Surface magnetometry of different samples from dyke 6A and 8A. Both the NRM and a 120°C demagnetization step were measured. Note the different scales for the Bz and therefore the different background colors. The measurement of sample 6A-50 is oversaturated, but it is included to show the difference in intensity of the magnetic sources compared to sample 6A-30.

were heated to 120°C to remove any potential secondary goethite interference.

A surprising result is the large difference between the two samples from dyke 6A. Note that the difference in background color in the figures of the two samples are caused by a different Bz-scale. Sample 6A-30 shows small magnetic sources with dipolar behavior, while sample 6A-50 shows a large, complex magnetic structure. The latter is probably caused by multi domain behavior from a single, large magnetic mineral. This result underlines the variation in size, shape, and abundance of the magnetic minerals throughout the dykes, as mentioned before (see geological setting).

The heating step of 120°C does not change the magnetic signal of the samples to a great extent. Although minor changes in magnetic direction or intensity are present, the samples do not demagnetize strongly from this heating step. This is somewhat in accordance with the observations of the bulk magnetic measurements (Fig. 2), because the LT component is not fully unblocked at 120°C. However, bulk sample 6A demagnetizes strongly before 120°C, something that is not directly visible from qualitative analyses of the QDM images.

Both samples from dyke 8A show scattered, small magnetic sources with both dipolar and quadrupolar behavior. The size and abundance of the magnetic sources is similar to those of 6A-30 although the sources in 8A are stronger.

Future

The surface magnetometry data from the QDM will be combined with the spatial and dimensional properties of the magnetic carriers in the samples. The latter were collected during a visit of the University of Oslo, where I used a nanoCT scanner with a resolution of approximately 300 nm to identify the shape, size, and position of the magnetic carriers in the samples. The combined data will be used to run an inverse model and determine the magnetic moment per individual grain. The NRM and various demagnetization steps that were measured with the QDM can then be used to separate several subsets of magnetic carriers that may provide interpretable information and hopefully shed light on the direction of the Archean magnetic field. In combination with the in-depth paleomagnetic study that Claire Nichols carried out on these samples, this will lead to a better understanding of the rock-magnetic properties of the Paleoarchean dyke swarm and the history of the Earth's magnetic field in general.

Acknowledgements to the IRM

For all their technical help with the QDM and teaching me how to use the QDM I would like to thank Peat Solheid and Michael Volk. I would like to thank the IRM for granting me the Magnetic Microscopy Fellowship and for giving me the chance to obtain the first QDM data for my PhD project. I would like to thank Dario Bilardello, Joshua Feinberg, and Maxwell Brown for our discussions on this and other paleomagnetic work.

References

Arai, T., Omori, S., Komiya, T., & Maruyama, S. (2015). Intermediate P/T-type regional metamorphism of the Isua Supracrustal Belt, southern west Greenland: The oldest Pacific-type orogenic belt?. Tectonophysics, 662, 22-39.

de Groot, L. V., Fabian, K., Béguin, A., Reith, P., Barnhoorn, A., & Hilgenkamp, H. (2018). Determining individual particle magnetizations in assemblages of micrograins. Geophysical Research Letters, 45(7), 2995-3000.

de Groot, L. V., Fabian, K., Béguin, A., Kosters, M. E., Cortés-Ortuño, D., Fu, R. R., ... & Barnhoorn, A. (2021). Micromagnetic tomography for paleomagnetism and rock-magnetism. Journal of Geophysical Research: Solid Earth, 126(10), e2021JB022364.

Nichols, C. I., Weiss, B. P., Eyster, A., Martin, C. R., Maloof, A. C., Kelly, N. M., ... & Cherniak, D. J. (2023). Possible Eoarchean records of the geomagnetic field preserved in the Isua Supracrustal Belt, southern west Greenland. Manuscript submitted for publication.

Nutman, A. P., Friend, C. R., Bennett, V. C., & McGregor, V. R. (2004). Dating of the Ameralik dyke swarms of the Nuuk district, southern West Greenland: mafic intrusion events starting from c. 3510 Ma. Journal of the Geological Society, 161(3), 421-430.

On the large-scale remagnetization of Ediacaran sedimentary units of West Gondwana: new insights from rock magnetism

Thales Pescarini
University of Sao Paulo and Yale University
thales.pescarini@usp.br

The large-scale remagnetization in Neoproterozoic sedimentary units of West Gondwana has been documented for decades (e.g., D'Agrella-Filho et al., 2000; Trindade et al., 2004; Font et al., 2006; Pescarini et al., 2022). This remagnetization appears to have been synchronous (~ 520 Ma) in different cratonic units composing the supercontinent, as indicated by the pole positions on the Apparent Polar Wander Path (APWP), following a period of an extremely weak geomagnetic field and the diversification of multicellular life (Bono et al., 2019; Lloyd et al., 2022). Despite being well-known, this event lacks a singular and integrated geological/geophysical explanation. Consequently, the potential physical origins and their connection to processes at the onset of the Phanerozoic remain limited. Additionally, the absence of this knowledge reduces the likelihood of extracting any primary paleomagnetic signal, which is scarce for the late Ediacaran.

My project aims to study rocks in different Ediacaran basins of West Gondwana through continental drilling (linked to the Geological Research Through Integrated Neoproterozoic Drilling project of the International Continental Drilling Program). The goal is to compre-

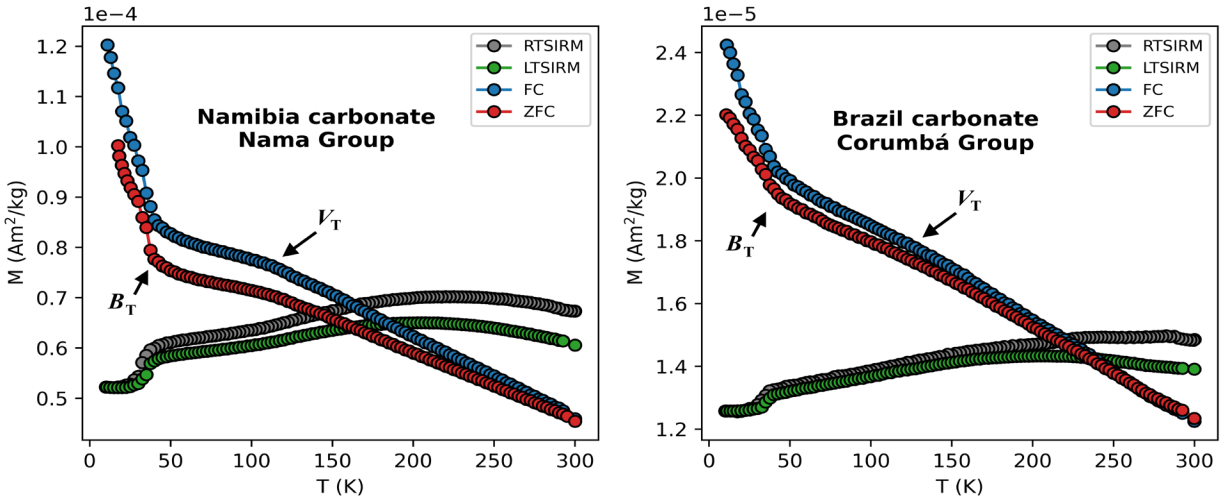

Figure 1: Examples of low-temperature cycles using the FC-ZFC-RTSIRM sequence on the Quantum Designs MPMS3 for Ediacaran carbonates from the Nama Group (left) and the Corumbá Group (right).

hensively characterize the magnetic and non-magnetic mineralogy and paleomagnetic directions to better understand the mechanisms of remanence acquisition and extract possible primary signals. In this context, my visit to the Institute for Rock Magnetism aimed to conduct sophisticated experiments in magnetic mineralogy, not explored in previous studies, to gain new insights into the mineralogical composition, grain size distribution, and domain structure of remanence carriers. For these experiments, I brought samples from the Nama Group

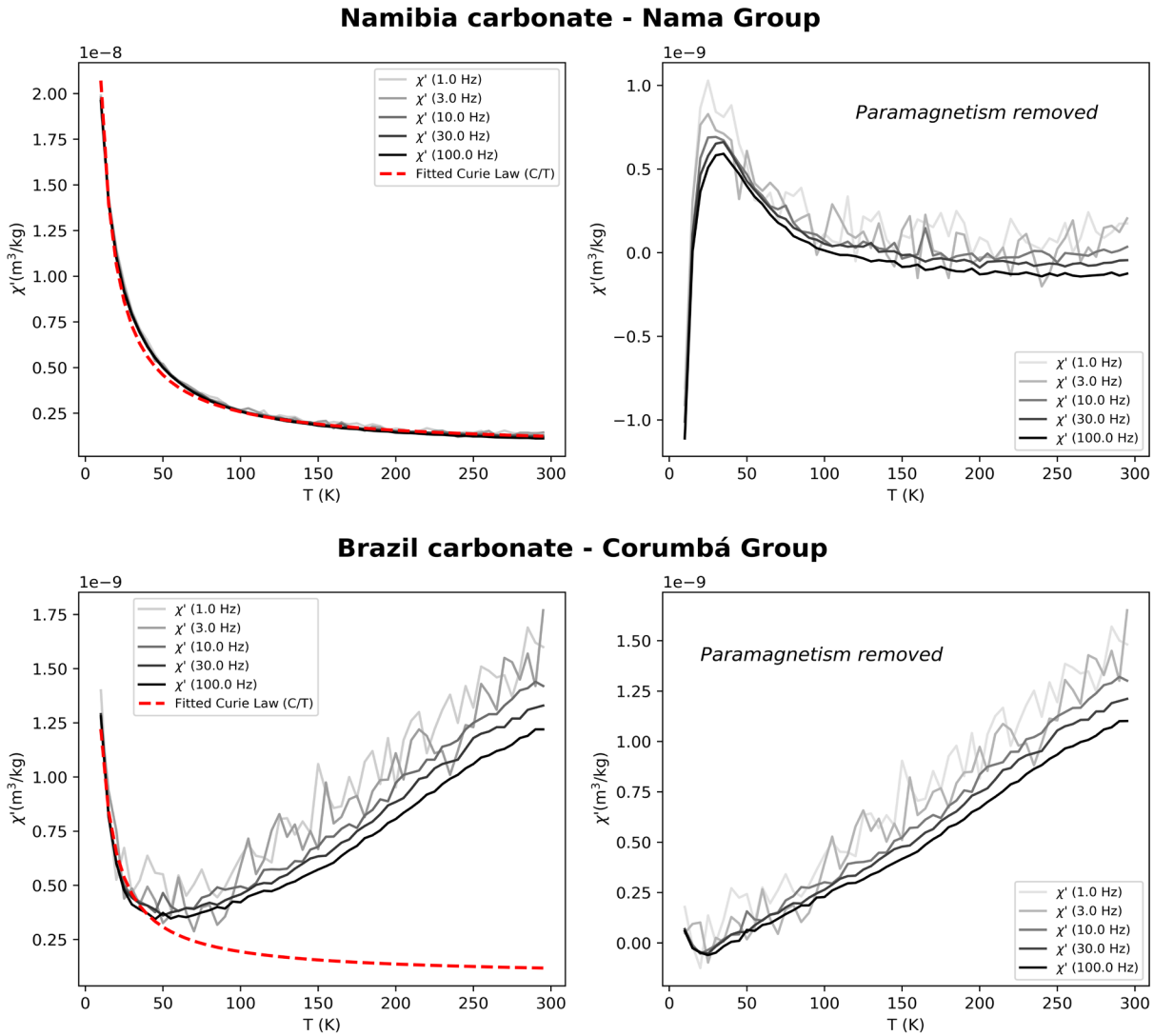

Figure 2: In-phase magnetic susceptibility (χ') as a function of temperature at different frequencies. The left panels display the raw data and the Curie Law fitted in red (χ'= C/T). The right panels show the result after subtracting the paramagnetic signal.

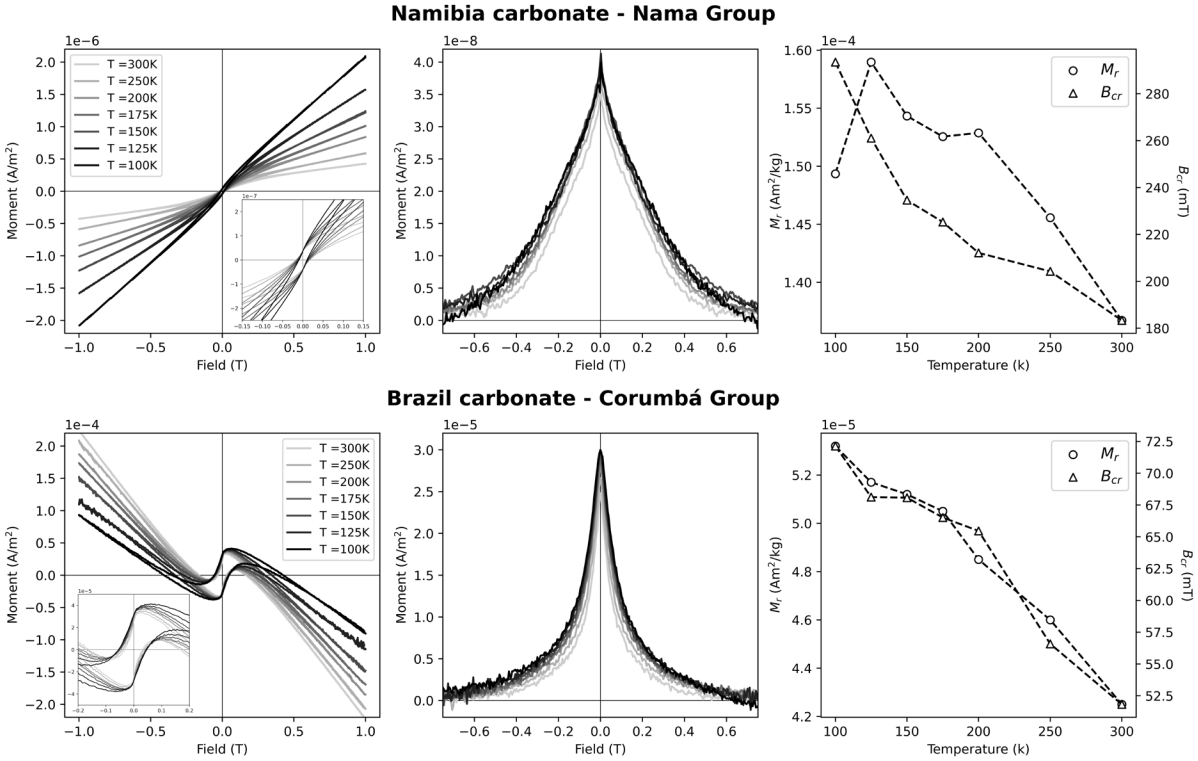

Figure 3: Hysteresis loops as a function of temperature. (left) Raw loops at different temperatures. Note the reduction of the wasp-waist effect with decreasing temperature. (center) Remanence at different temperatures. (right) Variation of M_r (circles) and B_{cr} (triangles) as a function of temperature.

(Namibia) and the Corumbá Group (Brazil), both encompassing the Ediacaran-Cambrian transition.

Low-temperature FC-ZFC-RTSIRM cycles were performed on the Quantum Designs MPMS3. This experiment shows equivalent curves for samples from both the Nama Group and the Corumbá Group (Fig. 1). In both sample sets, a sharp drop in magnetization around 30 K is observed in all curves, corresponding to the Besnus transition (B_T), characteristic of pyrrhotite ($Fe_{1-x}S_{x=0-0.2}$). A more discrete transition around 120 K is also noticeable, associated with the Verwey transition (V_T) of magnetite (Fe_3O_4). The suppression of V_T might be potentially linked to the degree of oxidation of magnetite (Ozdemir and Dunlop, 2010) or the ratio between the concentrations of pyrrhotite and magnetite. The position of the FC curve above the ZFC curve indicates the presence of magnetic grains with a single-domain (SD) structure. Additionally, the gap between the curves throughout the temperature range may suggest some contribution from goethite (FeO(OH)) (Strauss et al., 2013). This mineralogy aligns with the interpretation from thermal demagnetizations previously conducted in the laboratories of the University of São Paulo and Yale.

Also, on the MPSM3, magnetic susceptibility measurements were taken during progressive heating from 2 to 300 K at five AC frequencies (1, 3, 10, 30, and 100 Hz). Carbonates from the Nama Group and Corumbá Group exhibit different proportions of paramagnetic minerals, so a Curie Law, $\chi' = C/T$, was fitted and subtracted from the data to approximately isolate the ferromagnetic contribution (Fig. 2). Both results indicate a frequency-dependent susceptibility, commonly associated with thermally relaxing superparamagnetic (SP) particles. SP grains are common in remagnetized carbonates and are frequently associated with the authigenesis of magnetic particles in these rocks (e.g., Jackson and Swanson-Hysell, 2012). The presence of this type of material could also explain the well-marked viscous remanent magnetization (VRM) during demagnetizations. The frequency-dependent variation observed across almost the entire temperature range (only blocked below approximately 30 K) indicates a distribution of SP grains with different sizes.

Hysteresis loops and backfield curves at different temperatures (100, 125, 150, 175, 200, 250, and 300 K) were acquired on the Lakeshore 8600 VSM to distinguish the thermal stability of these particles. This is crucial as intrinsic hysteresis parameters (B_c, B_{cr}, M_s e M_{rs}) depend on the thermal state of the sample (e.g., Roberts et al., 2000; Pike et al. 2001). The obtained curves indicate a decrease in B_{cr} and M_r as the sample is heated from 100 to 300 K (Fig. 3). Conversely, the growth of these parameters in the opposite direction suggests progressive blocking of thermally relaxing particles towards a stable thermal state upon cooling. Additionally, the "wasp-waist" geometry in these curves becomes progressively attenuated with cooling, indicating that a mixture of remanence-carrying and SP particles becomes progressively blocked at lower temperatures (this effect is particularly evident in a carbonate from the Corumbá Group – see Fig. 3). This result aligns well with previous findings indicating a mixture of predominantly SP and SD grains.

Room temperature FORC diagrams were also obtained with measurements on the Lakeshore 8600 VSM

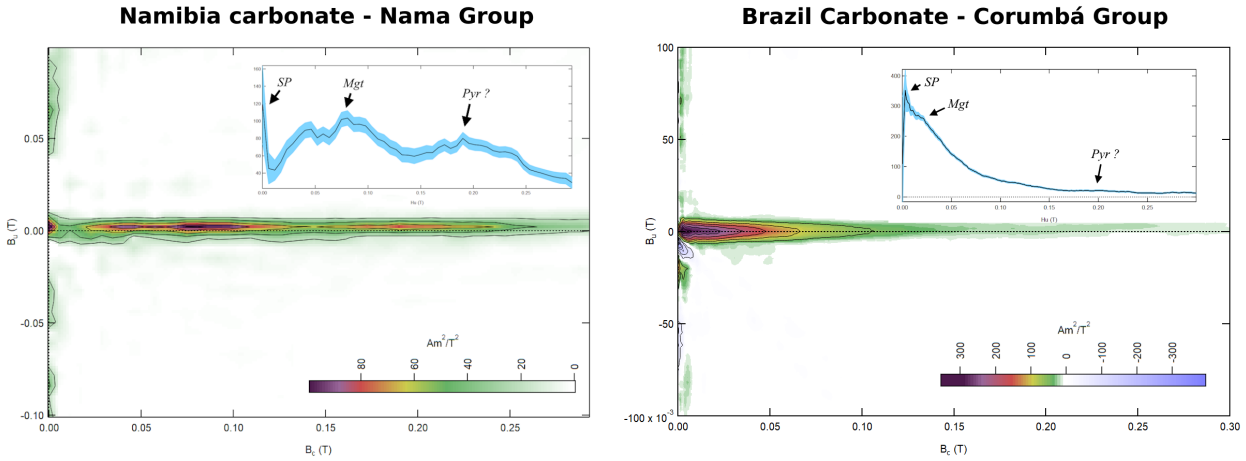

Figure 4: Representative FORC diagrams obtained for a carbonate from the Nama Group (left) and Corumbá Group (right). In the upper right corner of the diagrams, horizontal profiles ($B_u = 0$) are inserted with a 95% confidence interval in blue. SP = superparamagnetic particles, Mgt = magnetite, Pyr = pyrrhotite. VARIFORC parameters used for smoothing: (i) Nama: Sc0 = 4, Sb0 = 4, Sc1 = 6, Sb1 = 6, and λ = 0.1, (ii) Corumbá: Sc0 = 3, Sb0 = 4, Sc1 = 5, Sb1 = 5, and λ = 0.1.

to detail the magnetic mineralogy and domain structures. In these diagrams, a very well-defined central ridge can be observed in both carbonates from the Nama Group and the Corumbá Group (Fig. 4). Plotting a horizontal profile along the B_c axis ($B_u = 0$), different peaks in the FORC distribution can be distinguished, one near the origin ($B_c = 0$), one of low coercivity ($0 < B_c \leq 100$ mT), and one of high coercivity ($B_c \geq 150$ mT). These peaks align well with other experiments, suggesting a mixture of SP particles and SD magnetite and pyrrhotite.

Conclusion and Next Steps

Collectively, the conducted experiments indicate a highly similar magnetic mineralogy in temporally contemporaneous but spatially distant Ediacaran basins within the interior of West Gondwana. This mineralogy comprises SD pyrrhotite and magnetite, along with SP grains. Numerous questions and possibilities emerge from this mineralogical observation, particularly regarding the timing of mineral formation, the underlying genetic processes, and their relationship with paleomagnetic data.

The next steps will involve a more detailed analysis of rock magnetism data to delve deeper into these questions. We aim to connect these data with directional paleomagnetic information to explain the remagnetization processes geologically. Additionally, we plan to use this information as support in the attempt to extract primary signals from the samples. Finally, we expect to provide valuable insights into the geological evolution of these regions within West Gondwana during this critical period of the Earth's history.

Acknowledgments

I express my gratitude to the IRM staff for providing the opportunity to conduct these measurements and for the insightful conversations and suggestions that will undoubtedly critically contribute to the advancement of this work. Special thanks to Dario Bilardello, Peter Solheid, and Plinio Jaqueto for their assistance with equipment and measurements, and to Maxwell Brown for managing all aspects of my visit to the University of Minnesota. I extend my appreciation to FAPESP for funding this project through Grant #20/03347-5. IRM Visiting Fellowships are supported in part by NSF grants awarded to the IRM. Lastly, I thank the GRIND-ICDP team for their sampling efforts and management of these samples, as well as the University of São Paulo and Yale University where my research is conducted.

References

Bono R.K., Tarduno J.A., Nimmo F., Cottrell R.D., 2019. Young inner core inferred from Ediacaran ultra-low geomagnetic field intensity, Nat. Geosci., 12(2), 143–147. https://doi.org/10.1038/s41561-018-0288-0

D'Agrella-Filho, M.S., Babinski, M., Trindade, R.I.F., Schmus, W.R. Van, Ernesto, M., 2000. Simultaneous remagnetization and U–Pb isotope resetting in Neoproterozoic carbonates of the São Francisco Craton, Brazil. Precambrian Research. 99, 179–196.

Font, E., Trindade, R.I.F., Nédélec, A., 2006. Remagnetization in bituminous limestones of the Neoproterozoic Araras Group (Amazon craton): Hydrocarbon maturation, burial diagenesis, or both? Journal of Geophysical Research: Solid Earth. 111, 1–17. https://doi.org/10.1029/2005JB004106

Jackson, M., Swanson-Hysell, N.L., 2012. Rock magnetism of remagnetizated carbonate rocks: another look. In: Elmore, R. D., Muxworthy, A. R., Aldana, M. M., Mena, M. (eds). Remagnetization and Chemical Alteration of Sedimentary Rocks. Geological Society, London, Special Publications, 371. https://doi.org/10.1144/SP371.3

Lloyd, S.J., Biggin, A.J., Paterson, G.A., McCausland, P.J.A., 2022. Extremely weak early Cambrian dipole moment similar to Ediacaran: Evidence for long-term trends in geomagnetic field behaviour? Earth and Planetary Science Letters. 595, 117757.

Ozdemir, O., Dunlop, D. J. 2010. Hallmarks of maghemitization in lowt emperature remanence cycling of partially oxidized magnetite nanoparticles. J. Geophys. Res.-Solid Earth 115, https://doi.org/10.1029/2009jb006756

Pescarini, T., Trindade, R.I.F., Sant'Anna, L.G., 2022. Paleomagnetism of Maieberg cap carbonates, Namibia. Low latitude glaciations and supracontinental scale remagnetization events. IX Brazilian Symposium on Geophysics. Curitiba, PR/Brazil.

Pike, C. R., Roberts, A. P., Verosub, K. L., 2001. First-order reversal curve diagrams and thermal relaxation effects in

magnetic particles, Geophys. J. Int.,145, 721–730. https://doi.org/10.1046/j.0956-540x.2001.01419.x
Roberts, A. P., Pike, C. R., Verosub, K. L., 2000. FORC diagrams: A new tool for characterizing the magnetic properties of natural samples, J. Geophys. Res.,105, 28,461–28,475, https://doi.org/10.1029/2000JB900326.
Strauss, B. E. et al. The origin of magnetic remanence in stalagmites: Observations from electron microscopy and rock magnetism. Geochem. Geophys. Geosyst. 14, 5006–5025. https://doi.org/10.1002/2013GC004950
Trindade, R.I.F., D'Agrella-Filho, M.S.D., Babinski, M., Font, E., Brito, B.B., 2004. Paleomagnetism and geochronology of the Bebedouro cap carbonate: evidence for continental scale Cambrian remagnetization in the São Francisco craton, Brazil. Precambrian Research 128, 83–103. https://doi.org/10.1016/j.precamres.2003.08.010

Recent and Current Visiting Fellows

Period 2023b

Carl Richter
University of Lousiana at Lafayette: *High-resolution Environmental Magnetism and Paleomagnetism of IODP Site U1516A*

Julia Cartwright
University of Alabama: *Establishing the Extent of Space Weathering in Asteroid-Derived Meteorites*

Ji-In Jung
Stanford University: *Identification of Iron Oxides in Lunar Mare Basalts*

Jasmin Maunula
University of Helsinki: *Characterising Magnetic Minerals in Aerosol Dust in Helsinki, Finland*

Thales Pescarini
University of Sao Paulo: *Magneto- and cyclostratigraphy of the Nama Group, Namibia. Tectonic and geochronological implications for the Kalahari Craton in the Ediacaran - Cambrian transition*

Wentao Wang
Institute of Tibetan Pleateau Research, Chinese Academy of Sciences: *Isolating primary remanence to reconstruct the process of India-Asia collision*

Nitin Kadam
National Institute of Oceanography, Goa, India and National Museum of Natural History, Washington DC: *Tracing sediment source-to-sink processes along the continental margins of India using a magnetic mineral approach*

Current Articles

A list of current research articles dealing with various topics in the physics and chemistry of magnetism is a regular feature of the IRM Quarterly. Articles published in familiar geology and geophysics journals are included; special emphasis is given to current articles from physics, chemistry, and materials-science journals. Most are taken from ISI Web of Knowledge, after which they are subjected to Procrustean culling for this newsletter. An extensive reference list of articles (primarily about rock magnetism, the physics and chemistry of magnetism, and some paleomagnetism) is continually updated at the IRM. This list, with more than 10,000 references, is available free of charge. Your contributions both to the list and to the Current Articles section of the IRM Quarterly are always welcome.

Archeomag

Chen, Q., Q. R. Sun, L. S. Liao, W. Wang, and X. Q. Yang (2023), Magnetic characteristics of Chinese archaeological bricks and their implications for archaeomagnetism, Frontiers in Earth Science, 11, doi:10.3389/feart.2023.1272317.

Computation and Techniques

Heslop, D., J. L. Scealy, A. T. A. Wood, L. Tauxe, and A. P. Roberts (2023), A Bootstrap Common Mean Direction Test, Journal of Geophysical Research-Solid Earth, 128(8), doi:10.1029/2023jb026983.
Lima, E. A., B. P. Weiss, C. S. Borlina, L. Baratchart, and D. P. Hardin (2023), Estimating the Net Magnetic Moment of Geological Samples From Planar Field Maps Using Multipoles, Geochemistry Geophysics Geosystems, 24(7), doi:10.1029/2022gc010724.

Environmental Magnetism

Bao, X. J., S. H. Zhang, G. Q. Jiang, D. Chan, Y. Y. Hu, H. C. Wu, H. Y. Li, X. Q. Wang, and T. S. Yang (2023), Climate changes in the Cryogenian nonglacial epoch: A global synthesis with new findings from the Datangpo Formation in South China, Global and Planetary Change, 229, doi:10.1016/j.gloplacha.2023.104234.
Bin Hassan, M., G. Tagliaro, B. Harper, A. W. Droxler, E. Herrero-Bervera, Y. Yokoyama, A. Puga-Bernabeu, J. M. Webster, and L. Jovane (2023), A magnetic and geochemical approach to the changing sedimentation accumulation on the upper slope of the great barrier reef, northeastern Australian margin, Quaternary Science Reviews, 315, doi:10.1016/j.quascirev.2023.108230.
Bócoli, F. A., et al. (2024), Paleosol marked by contrasting formation processes: A pilot study using digital morphometrics in Southeastern Brazil, Catena, 234, doi:10.1016/j.catena.2023.107550.
Chen, L., Z. X. Yin, Y. L. Guan, Y. Z. Zhang, G. S. Li, and Z. X. Jiang (2023), Magnetic characteristics of sediments from the central basin of the South China Sea since the late Pleistocene: Implications for sediments provenance and evolution of the East Asian monsoon, Chinese Journal of Geophysics-Chinese Edition, 66(8), 3557-3575, doi:10.6038/cjg2022Q0418.
Cherin, M., et al. (2023), The dawn of the Late Villafranchian: Paleoenvironment and age of the Pantalla paleontological site (Italy; Early Pleistocene), Quaternary Science Reviews, 316, doi:10.1016/j.quascirev.2023.108279.
Dev, V., A. K. Sahu, S. Kumar, A. K. Rai, and S. S. Das (2023),

Paleoclimatic Influence on the Evolution of the Late Quaternary Clastic Sediments, Northwestern Arabian Sea, Journal of the Geological Society of India, 99(10), 1349-1360, doi:10.1007/s12594-023-2482-y.

Kulkarni, Y. R., S. J. Sangode, and D. C. Meshram (2023), Heavy Mineral and Mineral Magnetic Tracers of Basaltic versus Cratonic Weathering as Indicators of Spatio-temporal Shifts in the Monsoonal Intensity over Central Indian Region, Journal of the Geological Society of India, 99(9), 1191-1198, doi:10.1007/s12594-023-2451-5.

Lazaridis, G., L. Papadopoulou, V. Melfos, and P. Voudouris (2023), Iron oxide crusts in 2 hypogene caves in Greece, Journal of Cave and Karst Studies, 85(2), 51-61, doi:10.4311/2022es0100.

Lepre, C. (2023), Identifying Temperature and Moisture Controls on Fe Oxide Origins, Geophysical Research Letters, 50(17), doi:10.1029/2023gl102761.

Ni, Z. Y., B. Song, W. W. Sun, X. Q. Meng, X. D. Yang, and E. L. Zhang (2023), Anthropogenic environmental evolution of ganggeng lake in the East Asian monsoon marginal zone over the past century, Quaternary International, 670, 24-31, doi:10.1016/j.quaint.2023.09.015.

Wang, S. Y., Z. X. Chen, J. H. Yang, F. Y. Gao, W. D. Tian, X. Y. Ma, and D. S. Xia (2023), Magnetic properties of surface soils in the upper and middle reaches of the Yarlung Zangbo River Basin, southern Tibetan Plateau, and their environmental significance, Geophysical Journal International, 233(2), 1178-1190, doi:10.1093/gji/ggac511.

Wang, X. T., K. Jiang, Y. Liang, B. Su, J. G. Li, B. Y. Zheng, W. T. Liang, Z. X. Jiang, Q. Wang, and C. S. Jin (2023), Late Cretaceous paleoclimatic effects on the decreased dinosaur biodiversity in East Qinling, Chinese Journal of Geophysics-Chinese Edition, 66(9), 3774-3788, doi:10.6038/cjg2023R0032.

Xiong, J. G., Y. Z. Zhong, C. C. Liu, Q. R. Liu, H. P. Zhang, C. L. Deng, and Y. L. Li (2023), Mineral magnetic variation of the minle loess/palaeosol sequence of the late glacial to holocene period in the northeastern Tibetan Plateau, Geophysical Journal International, 235(2), 1624-1638, doi:10.1093/gji/ggad305.

Xue, P. F., L. Chang, and E. Thomas (2023), Abrupt Northwest Atlantic deep-sea oxygenation decline preceded the Palaeocene-Eocene Thermal Maximum, Earth and Planetary Science Letters, 618, doi:10.1016/j.epsl.2023.118304.

Zhou, M. L., C. X. Zhang, and Z. T. Guo (2023), Magneticenhancement mechanism of loess-soil sequence at Qinan during Middle Miocene and its paleoclimate significance, Chinese Journal of Geophysics-Chinese Edition, 66(8), 3316-3334, doi:10.6038/cjg2022Q0334.

Extraterrestrial and Planetary Magnetism

Barmatz, M., D. Steinfeld, J. Batres, H. Y. Hao, D. Rickman, and H. Shulman (2023), Microwave permittivity and permeability measurements on lunar simulants at low temperatures, Advances in Space Research, 72(10), 4503-4516, doi:10.1016/j.asr.2023.08.041.

Hoffmann, V. H., M. Junge, W. W. Schmahl, T. Mikouchi, K. Wimmer, and M. Kaliwoda (2023), NWA 15663 and PAIRS: magnetic susceptibility classification and comparison with selected meteorites and terrestrial mantle rocks, Meteoritics & Planetary Science, 58, A125-A125.

Tikoo, S. M., and J. Jung (2023), Establishing a Lunar Origin for Paleomagnetic Records in Apollo Samples, Geophysical Research Letters, 50(19), doi:10.1029/2023gl105152.

Fundamental and Applied Rock Magnetism

Kosterov, A., L. Surovitskii, V. Maksimochkin, S. Yanson, and A. Smirnov (2023), Tracing titanomagnetite alteration with magnetic measurements at cryogenic temperatures, Geophysical Journal International, 235(3), 2268-2284, doi:10.1093/gji/ggad360.

Pratama, A., et al. (2023), Magma storage conditions beneath Krakatau, Indonesia: insight from geochemistry and rock magnetism studies, Frontiers in Earth Science, 11, doi:10.3389/feart.2023.1128798.

Woods, T. W., J. M. Feinberg, K. Genareau, C. Park, H. Won, and Y. K. Hong (2023), Magnetic Properties of Lightning-Induced Glass Produced From Five Mineral Phases, Journal of Geophysical Research-Solid Earth, 128(9), doi:10.1029/2023jb026561.

Geomagnetism, Paleointensity and Records of the Geomagnetic Field

Alberti, T., F. Florindo, P. De Michelis, and G. Consolini (2023), Unveiling Geomagnetic Reversals: Insights From Tipping Points Theory, Geophysical Research Letters, 50(20), doi:10.1029/2023gl105646.

Chen, L., L. Zhou, J. B. Liu, Z. X. Yin, J. L. Zhang, Y. L. Guan, Y. Z. Zhang, Y. W. Hu, Y. Liu, and Z. X. Jiang (2023), A stacked record of relative palaeointensity for past 500 ka from western equatorial Indian Ocean sediments, Geophysical Journal International, 235(3), 2540-2555, doi:10.1093/gji/ggad383.

Shcherbakova, V. V., A. M. Pasenko, G. V. Zhidkov, V. P. Shcherbakov, and N. A. Aphinogenova (2023), An Ultralow Geomagnetic Field Intensity in the Mesoproterozoic Based on Studies of 1380 Ma Old Intrusive Bodies from the Udzha Aulacogen of the Siberian Platform, Izvestiya-Physics of the Solid Earth, 59(5), 682-703, doi:10.1134/s1069351323050105.

Tema, E., Y. Santos, R. Trindade, G. A. Hartmann, T. Hatakeyama, F. Terra-Nova, N. Matsumoto, J. Mitsumoto, and M. Gulmini (2023), Archaeointensity record of weak field recurrence in Japan: new data from Late Yayoi and Kofun ceramic artefacts, Geophysical Journal International, 233(2), 950-963, doi:10.1093/gji/ggac498.

Turner, G. M., and R. M. Corkill (2023), NZPSV11k.2023 and NZPSV1k.2023: Holocene palaeomagnetic secular variation master records for New Zealand, Physics of the Earth and Planetary Interiors, 344, doi:10.1016/j.pepi.2023.107093.

Yamazaki, T., J. X. Li, T. Shimono, and T. Kanamatsu (2023), Difference in Relative Paleointensity Recording Efficiency of Magnetic Mineral Constituents in a Sediment Core Off Chile, Journal of Geophysical Research-Solid Earth, 128(8), doi:10.1029/2023jb026816.

Magnetic Fabrics and Anisotropy

Joshi, G., P. Phukon, A. Agarwal, and A. K. Ojha (2023), On the Emplacement of the Impact Melt at the Dhala Impact Structure, India, Journal of Geophysical Research-Planets, 128(7), doi:10.1029/2023je007840.

Roperch, P., C. Kissel, F. Lagroix, G. Dupont-Nivet, A. Chauvin, F. Poblete, and J. Aminov (2023), Anisotropy of magnetic susceptibility impressed during rock magnetic procedures (AF, IRM) and information on the domain state of the magnetic carriers, Physics of the Earth and Planetary Interiors, 342, doi:10.1016/j.pepi.2023.107076.

Sun, X. X., Y. B. Tong, Z. Y. Yang, J. L. Pei, Z. J. Zhang, and L. F. Hou (2023), Identification of Growth Strata: New Insights From Anisotropy Corrected Paleomagnetic Data, Geophys-

ical Research Letters, 50(21), doi:10.1029/2023gl105625.
Tomek, F., I. Olsansk·, J. Trubac, J. Cerny, J. Rejsek, and L. Ackerman (2023), On the anatomy and structural control of a dyke swarm that fed caldera-forming ignimbrite eruptions, Journal of the Geological Society, 180(5), doi:10.1144/jgs2022-119.
Wack, M. R. (2023), Improved anisotropy of magnetic remanence results from vectorial readings using novel refinement method, Geophysical Journal International, 233(2), 1113-1123, doi:10.1093/gji/ggac500.

Magnetic Mineralogy and Petrology, Other

Bian, G., O. Ageeva, V. Roddatis, G. Habler, A. Schreiber, and R. Abart (2023), Oriented secondary magnetite microinclusions in plagioclase from oceanic gabbro, American Mineralogist, 108(9), 1642-1657, doi:10.2138/am-2022-8784.
Suttle, M. D., et al. (2023), Fossil micrometeorites from Monte dei Corvi: Searching for dust from the Veritas asteroid family and the utility of micrometeorites as a palaeoclimate proxy, Geochimica Et Cosmochimica Acta, 355, 75-88, doi:10.1016/j.gca.2023.06.027.
Wang, M. K., P. T. Yang, T. J. Chuang, C. C. Ou, and S. L. Wang (2023), Crystallization between (100) Goethite and (001) Orientation of Hematite - A Review, Clays and Clay Minerals, 71(2), 242-251, doi:10.1007/s42860-023-00242-8.
Watson, E. B., D. J. Cherniak, C. I. O. Nichols, and B. P. Weiss (2023), Pb diffusion in magnetite: Dating magnetite crystallization and the timing of remanent magnetization in banded iron formation, Chemical Geology, 640, doi:10.1016/j.chemgeo.2023.121748.

Paleomagnetism

Alva-Valdivia, L. M., J. F. Savian, C. R. TomÈ, A. Hernandez-Cardona, C. D. K. Tolotti, M. E. B. Gomes, and J. A. Gonz·lez-Rangel (2023), Full vector paleomagnetic estimation from the Parana-Etendeka Large Igneous Province, southern Brazil: Implications on the onset of Cretaceous Normal Superchron, Physics of the Earth and Planetary Interiors, 343, doi:10.1016/j.pepi.2023.107088.
Bhattacharya, A., A. Banerjee, and N. Sequeira (2023), The Central Indian Tectonic Zone: A Rodinia supercontinent-forming collisional zone and analogy with the Grenville and Sveconorwegian orogens, Geosphere, 19(5), 1300-1317, doi:10.1130/ges02597.1.
Cottrell, R. D., R. K. Bono, J. E. T. Channell, H. P. Bunge, and J. A. Tarduno (2023), No Late Cretaceous true polar wander oscillation and implications for stability of Earth relative to the rotation axis, Earth and Planetary Science Letters, 620, doi:10.1016/j.epsl.2023.118338.
Didenko, A. N., M. V. Arkhipov, Y. V. Taltykin, V. O. Krutikova, and E. A. Konovalova (2023), The Petro- and Paleomagnetic Characteristics of Gabbrodiorites from the Lower Amur Complex of the Zhuravlevka-Amur Terrane (the Sikhote-Alin Orogenic Belt), Russian Journal of Pacific Geology, 17(5), 457-474, doi:10.1134/s1819714023050020.
Efremov, I. V., and R. V. Veselovskiy (2023), PMTools: New Application for Paleomagnetic Data Analysis, Izvestiya-Physics of the Solid Earth, 59(5), 798-805, doi:10.1134/s1069351323050026.
Jensen, J. L., A. K. Ault, and J. W. Geissman (2023), Evaluating the Compatibility of Hematite (U-Th)/He Data and Hematite-Carried Secondary Magnetizations: An Example From the Colorado Front Range, Geochemistry Geophysics Geosystems, 24(9), doi:10.1029/2023gc010993.
Jutras, P., and J. Dostal (2023), Late Ordovician to Early Devonian tectono-magmatic prequel to the Acadian Orogeny in northeastern North America and the British Isles, Gondwana Research, 124, 378-400, doi:10.1016/j.gr.2023.08.002.
Klootwijk, C. (2023), Matching mid-to-latest Carboniferous pole path segments for eastern Australia and northern Armorica indicate a late Carboniferous Pangea-B configuration and a mid Carboniferous inertial interchange true polar wander event, Earth-Science Reviews, 244, doi:10.1016/j.earscirev.2023.104521.
Li, X., N. Suzuki, J. Meng, A. Matsuoka, P. O. Baumgartner, and C. S. Wang (2023), Constraints on the expanse of Greater India in the Early Cretaceous from radiolarians, Earth and Planetary Science Letters, 622, doi:10.1016/j.epsl.2023.118413.
Liu, P. F., S. Panovska, K. K. Zhang, and A. M. Hirt (2023), Assessing inclination flattening in the Holocene: insights from sediment data and global models, Geophysical Journal International, 233(2), 1271-1278, doi:10.1093/gji/ggac520.
Luoto, T., J. Salminen, S. Mertanen, S. A. Elming, and L. J. Pesonen (2023), New palaeoproterozoic palaeomagnetic data from Central and Northern Finland indicate a long-lived stable position for Fennoscandia, Geophysical Journal International, 235(2), 1810-1831, doi:10.1093/gji/ggad247.
Martin, C. R., O. Jagoutz, R. Upadhyay, J. A. van Tongeren, P. A. Mueller, and B. P. Weiss (2023), Paleomagnetic Constraint on the Age of the Shyok Suture Zone, Journal of Geophysical Research-Solid Earth, 128(10), doi:10.1029/2022jb026137.
Meert, J. G., S. R. Miller, A. Pivarunas, M. K. Pandit, P. Mueller, A. K. Sinha, G. Kamenov, S. Kwafo, and A. Singha (2024), Paleomagnetism and geochronology of the Gwalior Sills, Bundelkhand craton, Northern India Block: New constraints on Greater India assembly, Gondwana Research, 125, 29-48, doi:10.1016/j.gr.2023.08.004.
Michalski, K., G. M. Manby, K. Nejbert, J. Domanska-Siuda, and M. Burzynski (2023), Palaeomagnetic investigations across Hinlopenstretet border zone: from Caledonian metamorphosed rocks of Ny Friesland to foreland facies of Nordaustlandet (NE Svalbard), Journal of the Geological Society, 180(1), doi:10.1144/jgs2021-167.
Montheil, L., M. Philippon, P. Muench, P. Camps, B. Vaes, J. J. Cornee, T. Poidras, and D. J. J. van Hinsbergen (2023), Paleomagnetic Rotations in the Northeastern Caribbean Region Reveal Major Intraplate Deformation Since the Eocene, Tectonics, 42(8), doi:10.1029/2022tc007706.
Moreira, G., M. Ernesto, A. De Min, A. Marzoli, F. B. Machado, E. M. G. Vasconcellos, and G. Bellieni (2023), Paleomagnetism of the Penatecaua magmatism: The CAMP intrusive rocks in the Amazonas Basin, northern Brazil, Physics of the Earth and Planetary Interiors, 342, doi:10.1016/j.pepi.2023.107075.
Parashuramulu, V., E. Nagaraju, R. Shankar, N. R. Babu, and D. S. Sarma (2023), Paleogeography of India at similar to 1.8 Ga: New constraints from baddeleyite geochronology and paleomagnetism of mafic dykes from the Dharwar craton, Precambrian Research, 395, doi:10.1016/j.precamres.2023.107146.
Peskov, A. Y., I. P. Voinova, A. N. Didenko, S. V. Zyabrev, A. V. Kudymov, A. S. Karetnikov, and M. V. Arkhipov (2023), The Structural Position and the Petrogeochemical and Petropaleomagnetic Characteristics of Volcanic Rocks from the Nilan Terrane (the Junction Zone between the Mongol-Okhotsk and Sikhote-Alin Orogens) and Geodynamic Conclusions, Russian Journal of Pacific Geology, 17(5), 401-418, doi:10.1134/s181971402305007x.

Ren, Q., S. H. Zhang, T. Sukhbaatar, M. C. Hou, H. C. Wu, T. S. Yang, H. Y. Li, and A. Q. Chen (2023), Timing the Hegenshan Suture in the Central Asian Orogenic Belt: New Paleomagnetic and Geochronological Constraints From Southeastern Mongolia, Geophysical Research Letters, 50(20), doi:10.1029/2023gl104881.

Vaes, B., et al. (2023), A global apparent polar wander path for the last 320 Ma calculated from site-level paleomagnetic data, Earth-Science Reviews, 245, doi:10.1016/j.earscirev.2023.104547.

Wei, B. T., et al. (2023), Paleomagnetism of Late Triassic Volcanic Rocks From the South Qiangtang Block, Tibet: Constraints on Longmuco-Shuanghu Ocean Closure in the Paleo-Tethys Realm, Geophysical Research Letters, 50(19), doi:10.1029/2023gl104759.

Zhao, L., H. Tang, R. N. Mitchell, Q. L. Li, X. W. Zhou, and M. G. Zhai (2023), The Joining of North and South China During the Permian: Coherent Metamorphic Evidence From East Asia Orogenesis, Tectonics, 42(8), doi:10.1029/2023tc007916.

Zhao, P., Z. H. Jia, B. Xu, Y. Xu, T. Sukhbaatar, E. Appel, and Y. Chen (2024), Late Triassic initial closure of the Mongol-Okhotsk Ocean in the western segment: Constraints from sedimentological, detrital zircon ages and paleomagnetic evidence, Gondwana Research, 125, 110-129, doi:10.1016/j.gr.2023.08.007.

Stratigraphy

Gale, A., et al. (2023), The Global Boundary Stratotype Section and Point (GSSP) of the Campanian Stage at Bottaccione (Gubbio, Italy) and its Auxiliary Sections: Seaford Head (UK), Bocieniec (Poland), Postalm (Austria), Smoky Hill, Kansas (USA), Tepayac (Mexico), Episodes, 46(3), 451-490, doi:10.18814/epiiugs/2022/022048.

Gastaldo, R. A., and M. K. Bamford (2023), The influence of taphonomy and time on the paleobotanical record of the Permian-Triassic transition of the Karoo basin (and elsewhere), Journal of African Earth Sciences, 204, doi:10.1016/j.jafrearsci.2023.104960.

Hounslow, M. W., S. E. Harris, V. Karloukovski, and A. Mork (2022), Geomagnetic polarity and carbon isotopic stratigraphic assessment of the late Carnian-earliest Norian in Svalbard: evidence for a major hiatus and improved Boreal to Tethyan correlation, Norwegian Journal of Geology, 102, doi:10.1785/njg102-1-4.

Kodama, K. P., and F. J. Pazzaglia (2023), New paleomagnetic and rock-magnetic cyclostratigraphy-determined age, deposition rates, and processes for a part of the Calvert Cliffs (Miocene) passive margin deposits, Earth-Science Reviews, 245, doi:10.1016/j.earscirev.2023.104570.

Mattei, M., V. Fioramonti, G. P. Cavinato, F. Cifelli, I. Mazzini, M. Parotto, R. Sardella, and M. Sirna (2023), Magnetostratigraphy of the Collepardo Late Pliocene faunal assemblage (Early Villafranchian Triversa Faunal Unit), Ernici Mts., Central Italy, Italian Journal of Geosciences, 142(3), 398-410, doi:10.3301/ijg.2023.19.

Mitchell, R. N., and U. Kirscher (2023), Mid-Proterozoic day length stalled by tidal resonance, Nature Geoscience, 16(7), 567-+, doi:10.1038/s41561-023-01202-6.

Namier, N., et al. (2023), Comprehensive magnetic analysis of the tephras in Middle-Late Pleistocene loess records of Serbia, and implications for tephra identification, correlation and loess chronology, Quaternary Science Reviews, 313, doi:10.1016/j.quascirev.2023.108202.

Ruh, J. B., L. Valero, M. Najafi, N. Etemad-Saeed, J. Vouga, A. Mohammadi, F. Landtwing, M. Guillong, M. Cobianchi, and N. Mancin (2023), Tectono-Sedimentary Evolution of Shale-Related Minibasins in the Karvandar Basin (South Sistan, SE Iran): Insights From Magnetostratigraphy, Isotopic Dating, and Sandstone Petrology, Tectonics, 42(11), doi:10.1029/2023tc007971.

Zhang, M., J. X. Liu, Q. C. Zou, Z. Q. Yao, Y. G. Liu, and X. F. Shi (2023), Verification of the Arctic deep-sea magnetostratigraphy in enviromagnetic perspectives: A case study for sediment core ARC5-ICE4 on the Lomonosov Ridge, Chinese Journal of Geophysics-Chinese Edition, 66(7), 2983-2996, doi:10.6038/cjg2022Q0645.

Volcanology

Scarani, A., C. F. Faranda, A. Vona, F. Speranza, G. Giordano, S. G. Rotolo, and C. Romano (2023), Timescale of Emplacement and Rheomorphism of the Green Tuff Ignimbrite (Pantelleria, Italy), Journal of Geophysical Research-Solid Earth, 128(7), doi:10.1029/2022jb026257.

Save the Date!

2024 IRM Summer School in Rock Magnetism

We are pleased to announce that we plan to run the IRM summer school this June 3rd-12th. More information on the summer school's state-of-play will appear on our website:

https://cse.umn.edu/irm/2024-irm-summer-school-rock-magnetism

About the summer school:

The 10-day program is targeted at graduate students, advanced undergraduate students and postdocs in rock magnetism, paleomagnetism, and associated fields. Students will receive intensive instruction in rock magnetic theory and laboratory techniques. A daily schedule of lectures, hands-on laboratory measurements, and data processing will introduce students to the fundamentals of rock magnetism and the practical aspects of collecting and interpreting data responsibly. Instructors for the summer school will be primarily IRM faculty and staff. A special workshop on quantum diamond magnetometry will be led by Prof. Roger Fu (Harvard University).

Applications:

Applications are now open! Please visit our website for details on the application process and to complete the Google Form. The Deadline is February 15th, 2024.

For any questions about the Summer School, please contact Maxwell Brown at irm@umn.edu.

cont'd. from pg. 1...

where $\boldsymbol{k}_d$ is the vector of n directional susceptibilities measured in the given design. The resulting susceptibility tensor **k** can then be expressed in the form of its eigenvalues and eigenvectors, called principal susceptibilities ($k_1 \geq k_2 \geq k_3$) and principal directions, respectively. The AMS is traditionally characterized by the anisotropy parameters (sometimes also referred to as anisotropy factors) derived from the principal susceptibilities. The most frequently used anisotropy parameters are $L = k_1 / k_2$, $F = k_2 / k_3$, $P = k_1 / k_3$, $T = (2lnF / lnP) - 1$; the others are listed, for example, by Hrouda (1982) and Biedermann and Bilardello (2022).

Besides the estimated values of tensor elements and anisotropy parameters we also need to know how precisely they are estimated, which requires some redundancy in measurement. Repeated measurements can serve for this purpose, which is however rather laborious and time consuming. To avoid repeated measurements, Hext (1963) developed a method based on principles of classical statistics for the evaluation of symmetric second rank tensors, and susceptibility tensors especially, provided that the measuring protocol comprises measurements of directional susceptibilities in more than six independent directions. In the study by Hext (1963) and subsequent ones, special attention was paid to the measuring design, and rotatable designs were preferentially sought after. Jelínek (1977) further developed the Hext method for manual measurement of AMS in a rotatable design composed of 15 directions. Advances in automatization have made it possible to increase number of measured directions and Studýnka et al. (2014) presented a design consisting of 320 independent directions which is nearly rotatable.

Using the Hext approach, precision of the susceptibility tensor estimation can be assessed and consequently the confidence intervals of anisotropy parameters and confidence angles of principal directions can be determined. Nevertheless, this statistical treatment assumes that the measurement errors of individual directional susceptibilities are independent, random, and normally distributed. They also must not be large because the formulas for confidence intervals and angles were developed by linearization. If these assumptions are not fulfilled, or just for a comparison, a bootstrap method can be used (e.g., Constable and Tauxe, 1990).

In most cases, however, the linearization approach can be justified. In the following, we attempt to summarize its advantages, including the anisotropy/isotropy tests, factors controlling the precision of AMS determination and assessment of errors of anisotropy parameters and principal directions.

2. Tests for anisotropy and uniaxiality

The anisotropy/isotropy tests help to decide whether the measured anisotropy is an intrinsic property of the rock investigated or an instrumental artefact, and whether it is triaxial or uniaxial (oblate or prolate). The principle of the anisotropy test lies in verifying whether the differences between the calculated principal susceptibilities are large enough compared to the uncertainty in their estimate that is given by the measuring design and measuring errors. The practical implementation of the test is based on the analysis of variance. A ratio (F) of variances computed from principal susceptibilities and from directional susceptibilities has F-distribution on 5 and $n - 6$ degrees of freedom (Hext, 1963; Jelínek, 1977). If the ratio $F > F_{crit}$, where F_{crit} is a critical value at the chosen probability level (typically 95%), the hypothesis of isotropy is rejected and the measured specimen can be regarded as anisotropic. If $F < F_{crit}$, the measured specimen is either truly isotropic or it is so weakly anisotropic that this anisotropy is insignificant with respect to the measurement accuracy.

For example, it may happen that the same specimen measured with a very precise instrument is classified as statistically anisotropic, but can be classified as statistically isotropic if measured with a poorly accurate instrument. In addition, the result of the anisotropy test also depends on the probability level used, as the critical value increases with increasing probability. To avoid confusing complexity, it is reasonable to work with only one level of probability. For example, palaeomagnetism works with 95% level almost exclusively and we recommend using this level also in the case of the AMS. Similar F-tests as for anisotropy test exist to distinguish the triaxial AMS from the uniaxial AMS (oblate or prolate) (Jelínek, 1977).

The F-test results are crucial for further work. Namely, if the specimen shows to be statistically isotropic, its fabric interpretation should be avoided. Similarly, if the specimen is anisotropic but the AMS ellipsoid is rotational, only one principal direction should be further processed and interpreted, i.e., the minimum susceptibility direction (magnetic foliation pole) in the case of oblate AMS ellipsoids and the maximum susceptibility direction (magnetic lineation) in the case of prolate AMS ellipsoids.

3. Factors controlling the precision of the AMS determination

It is empirically known that the precision of the AMS determination primarily depends on the accuracy of the measurement of the directional susceptibility, but also on the number of measuring directions, and on the evenness of the distribution of the measuring directions in space. The effects of these factors were quantified through mathematical simulation of the measurement process and through the evaluation of the measurement precision using statistical theory (e.g., Hrouda and Pokorný, 2012; Guerrero-Suárez and Martín-Hernández, 2014; Hrouda et al., 2023). In the simulations, a certain susceptibility tensor ($\boldsymbol{\kappa}$) is considered, called the true tensor, and the vectors of the true directional susceptibilities along the measuring design are calculated as $\boldsymbol{\kappa}_t = \mathbf{A}\boldsymbol{\kappa}$. Each directional susceptibility is then encumbered by a measuring error generated by a random number generator according to Gauss normal distribution within the desired range, $\boldsymbol{\kappa}_d = \boldsymbol{\kappa}_t + \boldsymbol{\varepsilon}$. These directional susceptibilities are used as input data for calculating the model AMS. We will show

effects of several factors influencing the precision of the AMS determination.

Effect of the rotatability of the measuring design. The precision of the AMS determination depends, among other factors, on the orientation of the design of measuring directions with respect to the instrument coordinate system. Hext (1963) showed that there exist particularly advantageous designs giving rise to covariance matrices that are invariant with respect to any orthonormal transformation (rotation) of the coordinate system (see also Jelínek, 1977) and called them rotatable. In rotatable designs, there is no effect on the measurement precision. In non-rotatable designs, the effect depends on the degree of (non-)rotatability, which can be quantified by the rotatability coefficient $\boldsymbol{r} = (\mathbf{a}_{ii}^{T}\,\mathbf{V}\,\mathbf{a}_{ii})^{½}$ where $\mathbf{a}_{ij}$ is a matrix constructed from direction cosines and $\mathbf{V} = (\mathbf{A}^{T}\mathbf{A})^{-1}$ represents the covariance matrix (for details see Owens, 2000a).

The effect of the non-rotatability of the measuring design is illustrated in the following example that uses an artificial design composed of 10 directions (called Random 10) distributed relatively non-homogeneously and giving rise to strongly anisotropic rotatability coefficient (Figure 1a). Then, a model specimen is considered with $P = 1.5$ and $T = 0.1$ and measuring error of directional susceptibility characterized by standard deviation $\boldsymbol{\sigma} = 0.01$. The specimen was then gradually oriented according to the grid homogeneously covering the area of the unit-circle, and standard deviations of simulated principal susceptibilities and of P and T parameters were calculated as well as the angles defining the scatter of simulated principal directions. Figure 1b shows that the simulated standard error of the maximum principal susceptibility is direction dependent, and its distribution resembles the distribution of the rotatability coefficient (cf. Figures 1a, b).

Figure 1c presents results of the same simulations but using a rotatable Hext design composed of 10 directions (Hext 10). The interval of observed standard errors in maximum susceptibility is significantly narrower than in the case of the non-rotatable Random 10 design. The individual colours do not create conspicuous patterns, but are rather irregularly intermixed because in this design, the covariance matrix is direction independent, i.e., invariant with respect to the rotation of the coordinate system. Consequently, the errors can be regarded as solely due to measuring imprecision. The differences between *se k1* in Random 10 design and those in Hext 10 design can be interpreted as representing the effect of the anisotropy of rotatability coefficient in Random 10 design.

Effect of the number of measuring directions. This effect is illustrated on the example of the model specimen having $P = 1.5$ and $T = 0.1$, being measured with the error characterized by standard deviation $\boldsymbol{\sigma} = 0.01$, in two rotatable designs and one nearly rotatable one (Hext 10, Jelínek 15 and Studýnka 320, respectively). Figure 2 shows the variations of the simulated standard error of the maximum principal susceptibility as a function of the number of measuring directions. Theoretical curve for rotatable designs is added ($\boldsymbol{\sigma}\,\sqrt{(6/n)}$; Hext 1963) that fits the means of the simulated standard errors for Hext 10 and Jelínek 15 designs, while for the Studýnka 320 design it goes just below.

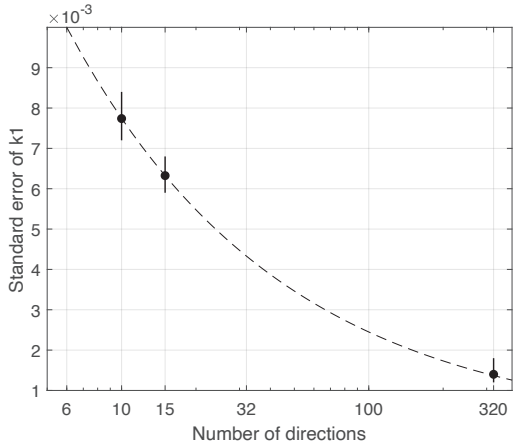

Figure 2: Simulated standard error of the maximum principal susceptibility for the designs Hext, Jelínek and Studýnka. Black dots are the means, vertical bars show the range (min to max). Dashed is theoretical curve for rotatable designs. (P = 1.5 and T = 0.1, $\boldsymbol{\sigma}$ = 0.01 used in simulations).

Initially, all the error rapidly decreases with increasing number of measuring directions, later ($n > 100$) the decrease is much slower. Consequently, the measuring designs with the number of measuring directions about several tens provide us with significantly lower standard errors than the designs with only several measuring directions. On the other hand, very high number of measuring directions, in the order of hundreds, results in only very small decrease of the simulated standard errors and confidence angles.

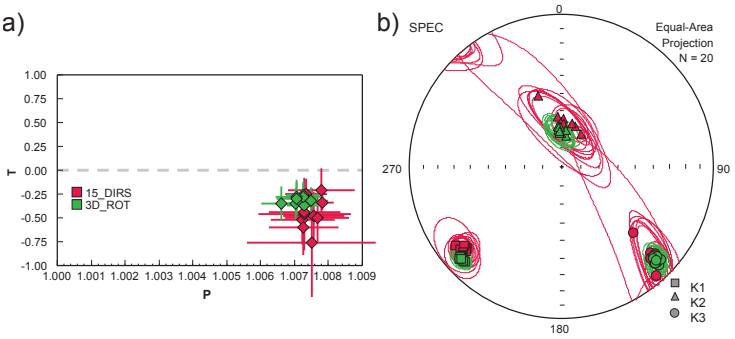

Figure 3: Ten repeated AMS measurements of the sandstone specimen (Flysch Belt of the Western Carpathians; $K_{mean} = 95 \times 10^{-6}$) measured using the MFK2 Kappabridge (H = 200 A/m, f = 976 Hz). Red (15_DIRS): Rotatable design of 15 directions, Green (3D_ROT): Nearly rotatable design of 320 directions. (a) P-T with confidence intervals. (b) Principal susceptibility directions with confidence angles, equal-area projection on lower hemisphere, specimen coordinate system.

The empirical validity of the above theory is illustrated in Figure 3. A weakly magnetic and very weakly anisotropic specimen of sandstone was repeatedly measured ten times manually using the rotatable design of 15 directions (Jelínek, 1977) and automatically with the nearly rotatable design of 320 directions (Studýnka et al. 2014). The confidence intervals of anisotropy param-

eters and confidence angles of the principal susceptibility directions are much larger in case of the 15-direction design than in the 320-direction design. Moreover, the results of repeated measurements are clearly better concentrated in the latter case. All this is in accordance with the theory.

Effect of the measurement error. In the simulations, three model specimens were considered having the following normed principal susceptibilities:
1.048 : 1: 0.952 (P = 1.1 and T = 0.024),
1.2 :1 : 0.8 (P = 1.5 and T = 0.1),
and 1.333 : 1 : 0.667 (P = 2.0 and T = 0.17).
Then, six relative measuring errors were considered,
σ = 0.001, 0.002, 0.003, 0.005, 0.0075, and 0.01.
Figure 4 shows the variation of the resulting simulated standard error of the degree of AMS (Figure 4a) and simulated shape parameter (Figure 4b) according to the measuring error and the degree of true AMS.

As seen in Figure 4a, the simulated error of P virtually linearly increases with increasing measuring error and the straight lines are the steeper the higher is the degree of true AMS considered. For common values of measuring error ($\sigma < 0.003$) the simulated standard error of the degree of AMS is mostly much less than 0.01, which is more than satisfactory for common magnetic fabric interpretations. Figure 4b shows the same variations for the T parameter. Again, the simulated standard error of T virtually linearly increases with increasing measuring error. The steepest straight line is that for P = 1.1, the least steep is that for P = 2.0. The simulated standard error of T is always less than 0.2, which is also quite satisfactory for common geological interpretations.

4. Errors in determination of anisotropy parameters and principal directions

Measuring susceptibility in more than six independent directions makes it possible to evaluate the errors in determining the principal susceptibilities and principal directions (e.g., Girdler, 1961; Jelínek, 1977; Tarling and Hrouda, 1993).

The basic parameter characterizing the precision of the AMS measurement is the standard error of the directional susceptibility estimated as (Jelínek, 1977)

$$s = \sqrt{\frac{1}{n-6}\sum_{i=1}^{N}(Km_i - Kf_i)^2}$$

where (Km_i) is the susceptibility measured in the *i-th* direction, Kf_i is the susceptibility in the same direction calculated from the fitted tensor and n is the number of measuring directions. The standard error of the principal susceptibilities is related to s. For rotatable designs, it is equal for all three principal values and given as $s_k = \sqrt{(6/n)}\, s$ (Hext, 1963; Jelínek, 1977). From the standard errors of principal susceptibilities, the standard errors of the anisotropy parameters can be calculated using the error propagation law (for principle see, e.g., Borradaile, 2003; for derived formulas see http://www.agico.com/downloads/documents/agicoprints/anisoerrors.pdf).

The knowledge of standard errors of the anisotropy parameters enables us to calculate the confidence intervals that inform us of the extent within which lies the true value on the probability level considered. The confidence interval for principal susceptibility on the 95% probability level is $k_i \pm s_k t_\alpha$, where t_α is 97.5% quantile of the Student distribution on n-6 degrees of freedom.

The confidence interval for the principal directions has the form of an ellipse on unit sphere whose semi-axes are characterized by confidence angles. Therefore, two angles are defined for each principal direction. In case of the rotatable measuring design, these two confidence angles are parallel to the principal planes of the susceptibility ellipsoid. For example, the confidence angle of the maximum susceptibility direction that lies in the plane passing through k_1 and k_2, is

$$e_{12} = \operatorname{atan}\left(s\sqrt{\frac{15F_\alpha}{2n}}\frac{1}{k_1 - k_2}\right)$$

where F_α is 95% quantile of F-distribution on 2 and n-6 degrees of freedom. The formulas for e_{23} and e_{13} error angles are analogous.

Formulas presented in this paragraph are valid for rotatable designs. It can be shown (Hrouda et al., 2023) that for designs that are close to rotatability, particularly designs with a high number of evenly distributed directions and devices constructed to ensure small errors of measurement, these formulas can be used with sufficient precision.

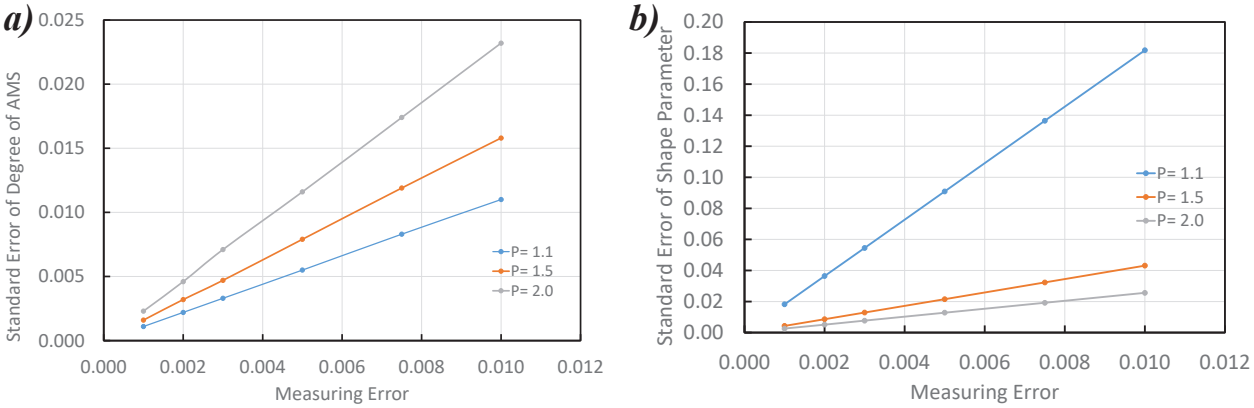

Figure 4: Variations of simulated standard error of (a) the degree of AMS and (b) the shape parameter according to the measuring error and the degree of true AMS.

5. Discussion and concluding remarks

It should be first emphasized that the above-described statistical methods of AMS measurements and evaluation of measurement precision provide us with the anisotropic properties of the specimen as a whole and do not inform us of individual AMS carriers and their sub-fabrics. It should also be noted that the above methods refer to statistics on the specimen level and not at the level of the sampling site or a groups of specimens. The representation of magnetic anisotropy by symmetric second rank tensor of susceptibility assumes a linear relationship between magnetization and magnetizing field, resulting in field-independent susceptibility. This is valid for diamagnetic and paramagnetic minerals by definition and empirically also for pure magnetite in weak fields. For other ferromagnetic minerals sensu lato (e.g., titanomagnetite, hematite, pyrrhotite) this assumption is valid only in very weak magnetizing fields in which the initial susceptibility is measured. For the latter minerals and fields used in common AMS meters, the use of the above linear theory is in principle incorrect. Nevertheless, the linear theory is so simple and elegant that the AMS researchers advocate using it provided that the errors introduced through linear fit to non-linear data are not too large (for details see, e.g., Hrouda, 2011).

The statistical methods for evaluating the precision of measurements of magnetic anisotropy developed by Hext (1963), Jelínek (1977), and Studýnka et al. (2014) and summarized in the present paper assume that the measuring protocol comprises redundant determinations of directional susceptibilities. This condition can be easily fulfilled in the case of automated measurement. For example, determining the AMS tensor by automatically measuring 320 directional susceptibilities in KLY5 and MFK2 Kappabridges takes only one and a half minute. This is a big advantage over laborious technique of repeated measurements or using low number measurement designs combined with a bootstrap method.

When measuring AMS of common rock types with modern sensitive instruments, the confidence angles are very small, less than 1°, often smaller than the size of the symbols depicting the principal directions in the graphical representation of the results. In this case there is no reason to plot the confidence areas. Only in either very weakly magnetic or very weakly anisotropic specimens like the example in Figure 5, the confidence areas and confidence interval of anisotropy parameters are larger and should be plotted.

Quite different case is often met when evaluating the results of the out-of-phase component of the AMS (opAMS) and the anisotropy of magnetic remanence (AMR) whose confidence intervals and confidence angles are usually much larger. In our opinion, the confidence angles should be always plotted in these cases. Unfortunately, they are almost never presented and the agreement between the principal directions cannot be reliably judged as well as the agreement between magnetic and mesoscopic fabric elements. Figure 6a shows an example for the agreement or disagreement of the principal susceptibility directions of the standard AMS (in fact the anisotropy of the in-phase component of susceptibility, ipAMS) and those of opAMS. The principal directions of both anisotropies differ and the corresponding confidence areas nowhere cross (note that confidence areas of ipAMS are small being hidden under the symbols depicting the principal directions). One can conclude that the principal directions of both anisotropies differ significantly, being probably carried by different mineral phases showing different sub-fabrics. Figure 6b shows three AMS and AMR results; again, the confidence areas of AMS are small, hidden under the symbols depicting the principal directions. The directions of AMS and AMR lineations (k_1) are very near, all lying within the confidence areas of the AMR lineations. The poles of AMR foliations (k_3) slightly differ from those of AMS foliations, all lying within the large confidence areas of

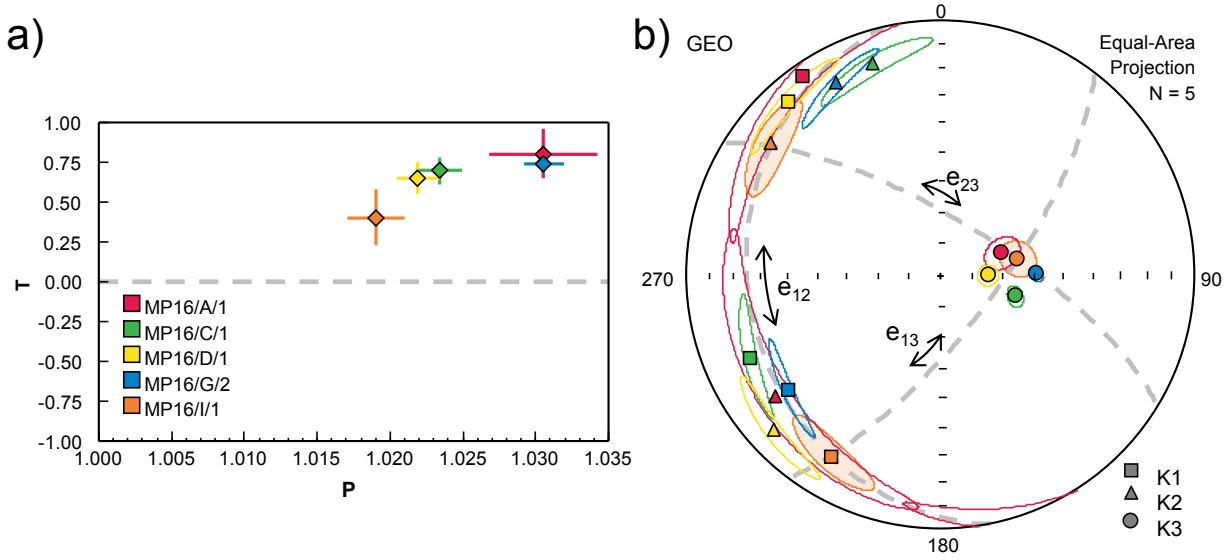

Figure 5: Colour-coded AMS results of five representative specimens from Arkose Sandstone (Hradec-Kyjovice Formation, Moravosilesian Kulm Basin). (a) AMS plot with confidence intervals for P and T parameters. (b) Equal-area projection of principal susceptibility directions with their confidence areas, geographical coordinate system. For the illustrative purpose, the confidence angles e_{12}, e_{23}, e_{13} are highlighted for specimen MP16/I/1. Data are courtesy of Filip Tomek (Tomek et al. 2019).

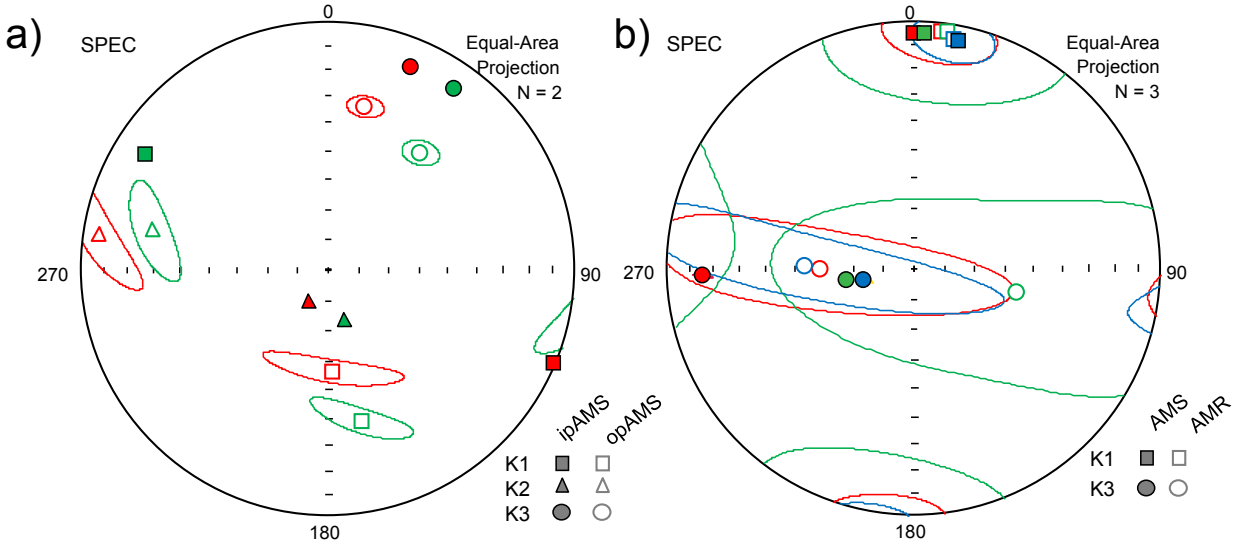

Figure 6: (a) Orientations of principal directions of ipAMS and opAMS and their confidence areas of two representative specimens of teschenite rock from Western Carpathians. (b) Orientations of AMS and AMR principal directions and their confidence areas of three representative specimens of rhyolite rock from Tharandter Wald Caldera, data are courtesy of Irena Olšanská (Olšanská et al. 2023). Both equal-area projections on lower hemisphere, specimen coordinate system.

the AMR foliation poles. One can conclude that the principal directions of both anisotropies probably reflect the magnetic fabric of the same mineral phases.

It can be concluded that evaluating the accuracy of magnetic anisotropy measurements at the specimen level is a prerequisite for reliable interpretation of the site-level magnetic fabric, for investigating the relationships between different magnetic anisotropy techniques as well as between magnetic and mesoscopic fabric elements. Modern instruments and recent advances in data processing programs provide us with these options automatically (e.g., Anisoft software, available free of charge at: http://www.agico.com/text/software/anisoft/anisoft.php).

Acknowledgement

The work on this paper was supported by AGICO, Inc., Charles University (through the Cooperatio Programme, Research Area GEOL), and Institute of Geology of the Czech Academy of Sciences (RVO 67985831).

References

Biedermann, A. and Bilardello, D., 2022. Practical Magnetism IX: Evaluating statistical significance of magnetic anisotropy data. IRM Quarterly, Vol. 32, 1, 11-15.

Borradaile G., 2003. Statistics of Earth Science Data. Springer-Verlag, Berlin, Heidelberg, New York, 351 pp.

Constable, C. and Tauxe, L., 1990. The bootstrap for magnetic susceptibility tensors. Jour. Geophys. Res., 95, 8383-8395.

Girdler, R.W., 1961. The measurement and computation of anisotropy of magnetic susceptibility of rocks. Geophys. J. R. astr. Soc., 5, 34-44.

Guerrero-Suárez, S. and Martín-Hernández, F., 2014. On the reliability of the AMS ellipsoid by statistical methods. Tectonophysics, 629, 75-86.

Hext, G.R., 1963. The estimation of second-order tensors, with related tests and designs. Biometrika 50, 353-373.

Hrouda, F., 1982. Magnetic anisotropy of rocks and its application in geology and geophysics. Geophys. Surv., 5, 37-82.

Hrouda, F., 2011. Anisotropy of Magnetic Susceptibility in Variable Low-Fields: A Review. In: E. Petrovský et al. (eds.), The Earth's Magnetic Interior, IAGA Special Sopron Book Series 1, DOI 10.1007/978-94-007-0323-0_19, © Springer Science+Business Media B.V. 2011.

Hrouda, F. and Pokorný, J., 2012. Modelling accuracy limits for frequency-dependent anisotropy of magnetic susceptibility of rocks and soils. Stud. Geophys. Geod., 56, 789-802.

Hrouda, F., Jezek, J. and Chadima, M., 2023. The effect of rotatability of measuring directions design on the precision of the determination of the anisotropy of magnetic susceptibility: mathematical model study. Phys. Earth Planet. Inter. – submitted.

Jelínek, V., 1977. The Statistical Theory of Measuring Anisotropy of Magnetic Susceptibility of Rocks and Its Application. Geofyzika n.p., Brno, Czech Republic. (http://www.agico.com/downloads/documents/agicoprints/statistical_theory.pdf)

Olšanská, I., Tomek, F., Chadima, M., Foucher, M.S., Petronis, M.S., 2024. Magnetic multi-fabrics as tools for understanding ignimbrite emplacement processes: An example from late-Variscan Tharandter Wald Caldera, Bohemian Massif. J. Struct. Geol., 178: doi.org/10.1016/j.jsg.2023.105012.

Owens, W.H., 2000a. Statistical applications to second-rank tensors in magnetic fabric analysis. Geophys. J. Inter., 142(2), 527-538.

Owens, W.H., 2000b. Error estimates in the measurement of anisotropic magnetic susceptibility. Geophys. J. Inter., 142(2), 516-526.

Studýnka, J., Chadima, M. and Suza, P., 2014. Fully automated measurement of anisotropy of magnetic susceptibility using 3D rotator. Tectonophysics, 629, 6-13.

Tarling D.H. and Hrouda F. 1993. The Magnetic Anisotropy of Rocks. Chapman & Hall, London, U.K., 217 pp.

Tomek, F., Vacek, F., Žák, J., Petronis, M.S., Verner, K. and Foucher, M.S., 2019. Polykinematic foreland basins initiated during orthogonal convergence and terminated by orogen-oblique strike-slip faulting: An example from the northeastern Variscan belt. Tectonophysics, 766, 379-397.

The IRM Quarterly

The *Institute for Rock Magnetism* is dedicated to providing state-of-the-art facilities and technical expertise free of charge to any interested researcher who applies and is accepted as a Visiting Fellow. Short proposals are accepted semi-annually in spring and fall for work to be done in a 10-day period during the following half year. Shorter, less formal visits are arranged on an individual basis through the Facilities Manager.

The *IRM* staff consists of **Subir Banerjee**, Professor Emeritus/Founding Director; **Bruce Moskowitz**, Professor/Director; **Joshua Feinberg**, Professor/Associate Director; **Maxwell Brown, Peat Sølheid** and **Dario Bilardello**, Staff Scientists.

Funding for the *IRM* is provided by the **National Science Foundation** and the **University of Minnesota**.

UNIVERSITY OF MINNESOTA

The *IRM Quarterly* is published four times a year by the staff of the *IRM*. If you or someone you know would like to be on our mailing list, if you have something you would like to contribute (*e.g.*, titles plus abstracts of papers in press), or if you have any suggestions to improve the newsletter, please notify the editor:

Dario Bilardello
Institute for Rock Magnetism
University of Minnesota
150 John T Tate Hall
116 Church Street SE
Minneapolis, MN 55455-0128
phone: (612) 624-5049
e-mail: dario@umn.edu
www.cse.umn.edu/irm

IRM